Hindawi Publishing Corporation
EURASIP Journal on Wireless Communications and Networking
Volume 2009, Article ID 131576, 11 pages
doi:10.1155/2009/131576

Research Article

Real-Time Propagation Measurement System and Scattering Object Identification by 3D Visualization by Using VRML for ETC System

Minseok Kim,[1] Jun-ichi Takada,[1] Tetsuo Ando,[2] and Ryuji Soma[2]

[1] *Graduate School of Engineering, Tokyo Institute of Technology, Tokyo 152-8552, Japan*
[2] *Nippon Expressway Research Institute Company Limited, 1-4-1 Tadao, Machida-shi, Tokyo 194-8508, Japan*

Correspondence should be addressed to Minseok Kim, mskim@ieee.org

Received 25 April 2008; Accepted 27 September 2008

Recommended by Eylem Ekici

In the early deployment of electric toll collecting (ETC) system, multipath interference has caused the malfunction of the system. Therefore, radio absorbers are installed in the toll gate to suppress the scattering effects. This paper presents a novel radio propagation measurement system using the beamforming with 8-elmenet antenna array to examine the power intensity distribution of the ETC gate in real time without closing the toll gates that are already open for traffic. In addition, an identification method of the individual scattering objects with 3D visualization by using virtual reality modeling language will be proposed and the validity is also demonstrated by applying to the measurement data.

1. Introduction

In Japan, electric toll collecting (ETC) system in the highway, an application of dedicated short range wireless communication (DSRC) 5.8 GHz interactive radio communication, has been introduced since 2001 and it is currently installed in above 70% of the toll gates. ETC services started in Japan, with the following aims: to alleviate traffic congestion near toll gates, to enhance convenience for drivers by eliminating the need to handle cash, and to reduce management cost. The ETC system in Japan handles the complicated system of tolls in which different amounts are charged according to the type of vehicle and distance traveled. The toll mechanism is illustrated in Figure 1 [1].

In the early deployment of ETC system, multipath interference has caused the malfunction of the system. Therefore, electromagnetic absorbers are installed on some objects, such as canopy, sidewall, poles, and so forth, in the toll gate to suppress the scattering. Thanks to the electromagnetic absorbers [2], the malfunction significantly decreased but the periodical investigation into the corrosion is still required for the maintenance and replacement after the installation. Since the measurement has been taken only for the spatial distribution of the power of the combined signal in conventional method using a spectrum analyzer, the sufficient examination has not been carried out from the diagnostic point of view.

In such kind of examination, the simulation approach based on geometric optics theory should be necessarily introduced, but the scattering process by irregular objects is very complicated. Eventually the on-site measurement is indispensable for an accurate diagnosis. We have studied the identification of the propagation paths using digital signal processing with array antennas to investigate the multipath propagation mechanism precisely [3, 4]. In our previous studies, the measurement method using a vector network analyzer (VNA) and X-Y-Z positioner was employed as shown in Figure 2. However, as a matter of fact, it was not straightly applicable in the toll gates that have been already open for traffic because it generally required closing the toll gates for several hours.

This paper proposes a novel radio propagation measurement system for the ETC gates. The most significant feature of this system is that the measurement can be made on the vehicle passing through the gates using the real ETC signal transmitted from the ETC roadside station, thus there is no need to close the toll gates. In practice, it is greatly useful to maintain and manage the toll gates already

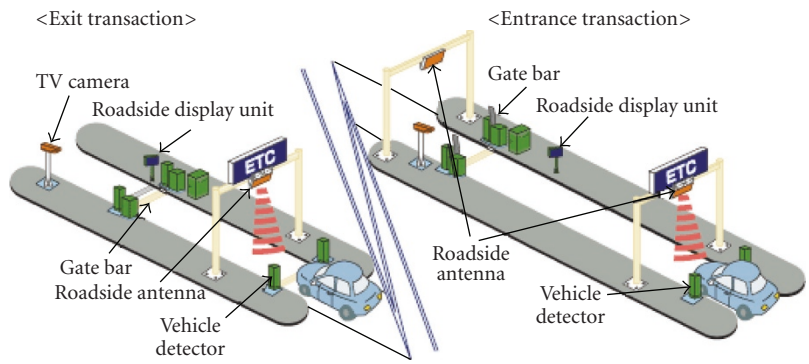

Figure 1: Mechanism of ETC [1].

Figure 2: Previous measurement at ETC gate; it generally required to close the toll gates.

open for traffic. This system can identify the individual scattering object by using the power intensity around the ETC gate with 3D (three-dimensional) visualization method using VRML (virtual reality modeling language) as well as the spatial power distribution in real time. In this paper, the measurement principle and the developed system configuration will be described. The evaluation by the field experiment will be presented as well.

2. Measurement System

2.1. Hardware Setup. The signal processing in this system was implemented basically on multiple-input multiple-output (MIMO) SDR (software defined radio) testbed system of Tokyo Institute of Technology [5] as shown in Figure 3. It consists of eight channels of receivers and ADCs, five large scale FPGAs (field-programmable gate arrays) for realtime processing and the buffer first-in first-out (FIFO) memory, and CPU operated by Microsoft Windows system on which the developed measurement software runs.

Figure 4 shows the system block diagram. The eight-element uniform antenna array is employed with two dummy elements at both end of the array and each element is a circularly polarized microstrip antenna which is currently

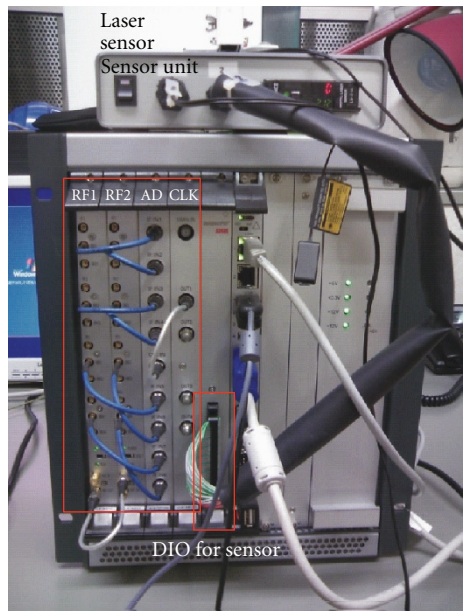

(a) MIMO-SDR testbed

(b) Measurement setup in the vehicle

Figure 3: Measurement equipment.

used for ETC. The antenna is installed on the rooftop of the measurement vehicle as shown in Figure 5. The ETC signal received in the antenna array at RF frequency of 5.8 GHz is downconverted into low IF in the receivers. Then the IF

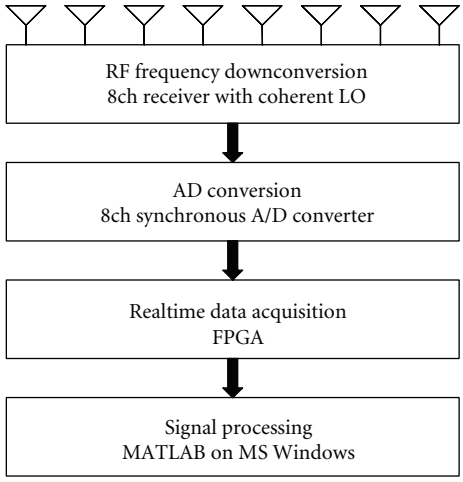

Figure 4: System block diagram.

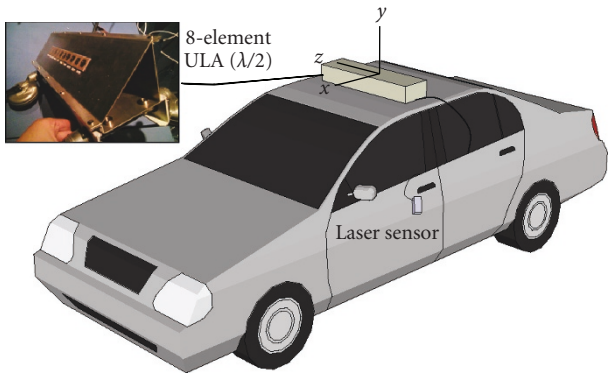

Figure 5: Array antenna mounted on measurement vehicle.

signals are synchronously sampled by ADCs and stored in the memory implemented on FPGAs. The data processing is carried out by software on CPU. Table 1 describes the specifications of this system.

2.2. Measurement Concept. In the measurement, this system captures the data in burst-wise manner at each time frame in a moving vehicle. The vehicle loading this system usually passes through the toll gate at constant speed of 20 km/h as shown in Figure 6. In the measurement, the laser sensor is used to trigger for the start and end positions of the measurement because it is not assumed for the measurement vehicle to be a dedicated one. The system captures the data at every equitime interval along the running path until the end-trigger is detected. The realtime data acquisition was implemented on FPGAs and the capacity is 28 K samples per channel for single measurement. Figure 7 shows capturing flow of the burst frame data for the length of the measurement area, 13 m, where the single frame includes 100 samples to estimate a correlation matrix. The data is usually captured at any arbitrary asynchronous timing to the ETC signal transmission. That means that the signal captured at valid timing should only be chosen.

Table 1: System specification.

Array antenna	
Array geometry	8-element uniform linear array
Element spacing	25.77 mm (0.5 wavelength)
Antenna element	Circularly polarized MSA
RF block	
RF frequency	5.470~5.875 GHz
Maximum input power	+10 dBm
Noise figure	16 dB
Gain controller	0~ + 80 dB
Bandwidth	40 MHz max.
Output signal	Baseband or low IF
ADC block	
Input frequency	100 kHz ~200 MHz
Sampling frequency	20~80 MHz
Quantization bit	14 bit
FIFO	128 k sample/ch
FPGA block	
FPGA	Xilinx Virtex-II 2 M gate ×5
FPGA memory	about 28 k sample/ch

Table 2: ETC signal specification (ARIB STD-T75 [6]).

Modulation	ASK split phase coding (binary, duty 1/2)
Symbol rate	1024 k symbol/s
Carrier frequency	D1: 5.795 GHz, D2: 5.805 GHz
Roll off filter	cosine roll off, $\alpha = 1$
Occupied bandwidth	4.4 MHz
Rx power range	−39.6~ − 60.5 dBm
Rx threshold	−70.5 dBm

3. Signal Processing

3.1. Preprocessing. The transmitted RF signals from the roadside antenna are received in array antenna. The signal specification is described in Table 2 [6]. The whole signal band including two DSRC downlink channels of D1 and D2 for ETC systems is downconverted into intermediate frequency (IF) of 10 MHz. The signal $x_m(t)$ of the mth element is written by

$$x_m(t) = A_m \cos(2\pi f_{\mathrm{IF}} t + \phi_m)\left[\sum_{k=-\infty}^{\infty} s(t - kT_s, b_k)\right] + n_m(t), \tag{1}$$

where A_m and ϕ_m denote the amplitude and phase of the propagation transfer function. b_k, $s(t, b)$ and T_s are the kth symbol value (0 or 1), the waveform for the symbol b and the symbol duration, respectively. f_{IF} means IF center frequency. $n_m(t)$ denotes additive white Gaussian noise. IF signals are digitized at the sampling rates of 80 MHz. This system can process two channels of ETC signals at the same time without changing receiver's local oscillator (LO) frequency because the receiver has broad bandwidth of 40 MHz. The system

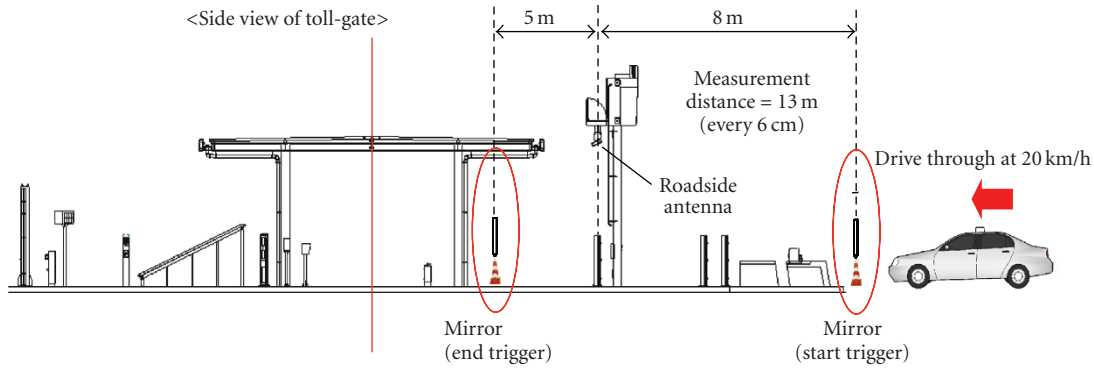

Figure 6: Measurement concept; the vehicle loading the system usually passes through the toll gate at constant speed of 20 km/h capturing the data in burst-wise manner.

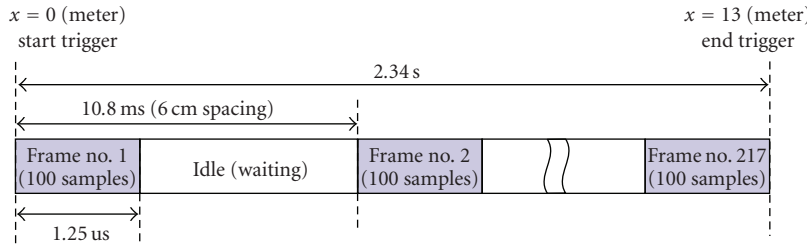

Figure 7: Capturing flow of the burst frame data; the length of the measurement area: 13 m.

Table 3: System setup parameters.

Receiver LO frequency	5.790 GHz
Sampling frequency	80 MHz

setup parameters are presented in Table 3. In digital signal processing, a desired channel of the two is selected by lowpass filtering for D1 or bandpass filtering for D2. The IF center frequency is downconverted to DC, where the complex signals can be obtained for signal processing afterward. The complex signal is denoted by $\overline{x}_m(t)$ hereafter.

3.2. Beamforming. The estimated correlation coefficient $\hat{r}_{mm'}$ for $r_{mm'}$ between mth and m'th channels is written by

$$\begin{aligned}\hat{r}_{mm'} &= \frac{1}{N}\sum_{n=0}^{N-1}\overline{x}_m(nT+t_0)\overline{x}_n^*(nT+t_0)\\ &\simeq A_m A_{m'}\exp\{j(\phi_m-\phi_{m'})\}+\sigma_{\mathrm{n}}^2,\end{aligned} \tag{2}$$

where $\overline{x}_m(t)$ and σ_{n}^2 are complex signal generated from $x_m(t)$ and average power of the receiver noise, respectively.

In this system, the 1D beamforming on the plane that determined by the axis of the antenna array and the directional vector for the source is used for stable operation with limited number of antenna elements. This system aims the scattering object identification, thus it needs high reliability rather than high resolution. The beamforming is computed with the estimated correlation matrix at every observation point by

$$P(\theta) = \mathbf{w}^H(\theta)\hat{\mathbf{R}}\mathbf{w}(\theta), \tag{3}$$

where θ is an angle of arrival (AoA) from the array axis. $\mathbf{w}(\theta)$ denotes the weight vector steering toward θ direction, ideally, written as

$$\mathbf{w}(\theta) = \mathbf{w}_{\mathrm{a}} \odot \mathbf{a}(\theta), \tag{4}$$

where $\odot$ denotes Hadamard product operator. The mode vector $\mathbf{a}(\theta) = [a_1(\theta), a_2(\theta), \ldots, a_M(\theta)]^T \in \mathbb{C}^{M\times 1}$, where

$$a_m(\theta) = \exp\left\{j\frac{2\pi}{\lambda}z_m\cos\theta\right\}. \tag{5}$$

The position of the mth element, z_m is written by

$$z_m = \left(m - \frac{M+1}{2}\right)d, \tag{6}$$

where M and d denote the number of antennas (=8, herein) and the spacing between antennas, respectively and $\mathbf{w}_{\mathrm{a}}$ is the window coefficients vector. In order to reduce the sidelobe gain of the uniform beampattern, we employed the Hamming window $\mathbf{w}_{\mathrm{a}} = [w_{\mathrm{a}1}, w_{\mathrm{a}2}, \ldots, w_{\mathrm{a}M}]^T \in \mathbb{Z}^{M\times 1}$ in (4) as

$$w_{\mathrm{a}m} = 0.54 + 0.46\cos\frac{2\pi z_m}{Md}. \tag{7}$$

Figure 8 shows the beamforming result when the wave is impinging from $\theta = \pi/2 = 90^\circ$. Dynamic range of more than 40 dB is achieved. The angular resolution results in nearly 20° at around bore sight direction as shown in Figure 9.

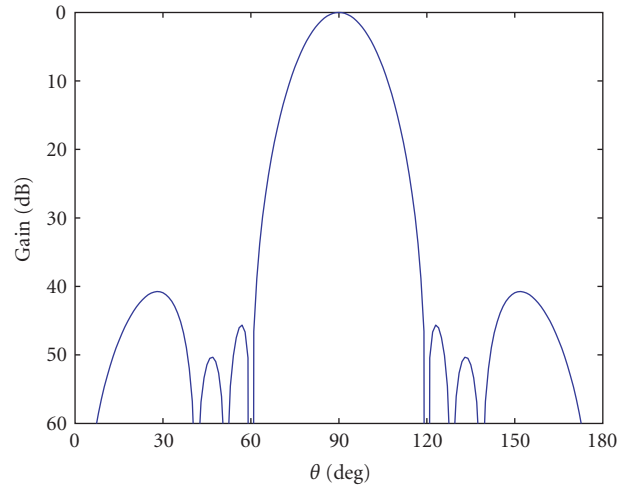

Figure 8: Beamforming output of proposed system (angle of arrival = 90°).

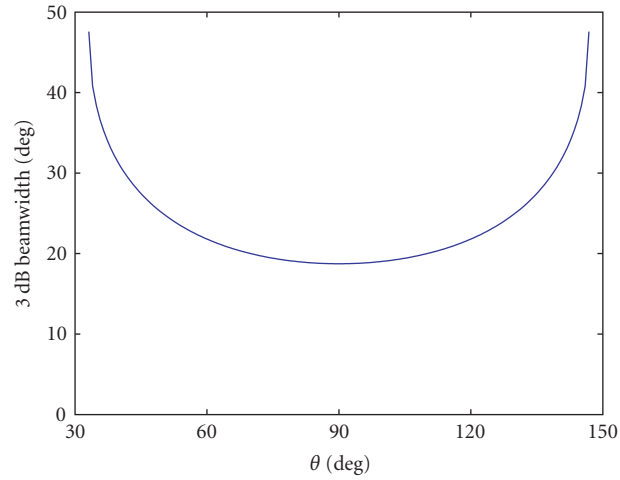

Figure 9: 3 dB beamwidth of proposed system.

3.3. System Calibration. So far each antenna in an antenna array has been assumed to have an ideal omnidirectional property. However, in general, the actual response of the antenna array significantly deviates from the assumed ideal model. In addition, the amplitude and phase response for each channel in the multichannel receiver has been assumed to be identical. But in reality, it is not feasible. Therefore it is generally needed to measure the actual responses of the antennas and receivers in advance. It is called *system calibration*.

Considering the responses of array antenna and RF cable do not vary so much over time and space, total responses including those of receivers are measured in a radio anechoic chamber. Strictly speaking, the radiation pattern of each antenna element, mutual coupling and deviation among RF cables should be properly calibrated. As far as this system employs a linear antenna array, the deviation of the radiation pattern of each antenna element cannot be eliminated by calibration processing since there exists cone ambiguity in the beamforming. Therefore we measured the calibration data only on the plane determined by the directional vector toward the maximum radiation pattern and the array axis. Moreover, the receiver is greatly affected by temperature, thus on-site calibration is necessary. For receiver calibration, we used the one-to-eight power divider calibrated by a vector network analyzer in advance.

For M-element array, the calibration data for θ_k direction, $\overline{\mathbf{X}}_{\text{cal}}^{\theta_k}(t)$, which includes an array manifold, $\hat{\mathbf{a}}(\theta_k)$, is written by

$$\overline{\mathbf{X}}_{\text{cal}}^{\theta_k}(t) = \hat{\mathbf{a}}(\theta_k)\cdot s_{\text{cal}}(t) + \mathbf{n}(t) \quad (k = 1, 2, \ldots, K), \tag{8}$$

where $s_{\text{cal}}(t)$, $\mathbf{n}(t) \in \mathbb{C}^{M\times 1}$, and K denote a reference signal for calibration, a noise vector with zero mean and variance of σ_{n}^2 and the number of calibration data, respectively. In this study, the calibration data at every 5° were collected.

The array manifold in (8) can be considered by dividing as

$$\hat{\mathbf{a}}(\theta) = \text{diag}(\boldsymbol{\Gamma}_{\text{cal}})\cdot\mathbf{b}(\theta), \tag{9}$$

where $\boldsymbol{\Gamma}_{\text{cal}} = [\Gamma_{\text{cal},1}, \Gamma_{\text{cal},2}, \ldots, \Gamma_{\text{cal},M}]^T \in \mathbb{C}^{M\times 1}$ and $\mathbf{b}(\theta) \in \mathbb{C}^{M\times 1}$ denote the receiver response vector and the antenna response vector including the cable response, respectively. diag($\mathbf{v}$) is an operator that produces a diagonal matrix and simply puts the vector $\mathbf{v} \in \mathbb{C}^{M\times 1}$ on the main diagonal. In order to improve the angle resolution, some interpolation techniques for discrete array manifold have been frequently introduced. In this study, an efficient technique based on Fourier series expansion of the array manifold was employed [7]. It divides the array manifold into EADF (effective aperture distribution function) matrix, $\mathbf{G} \in \mathbb{C}^{M\times L}$, and Vandermonde vector, $\mathbf{u}(\theta) \in \mathbb{C}^{L\times 1}$ as

$$\text{diag}(\boldsymbol{\Gamma}_{\text{cal}})\cdot\mathbf{b}(\theta) = \mathbf{G}\cdot\mathbf{u}(\theta), \tag{10}$$

where

$$\mathbf{u}(\theta) = \frac{1}{L}\left[e^{j((L-1)/2)\theta}, \ldots, 1, \ldots, e^{-j((L-1)/2)\theta}\right], \tag{11}$$

where L is the mode number to be properly chosen. By using the angle independent EADF matrix, the continuous array responses can be obtained.

However, the receiver response on the calibration data measurement, $\boldsymbol{\Gamma}_{\text{cal}}$, is usually changed in the measurement site, thus it should be also measured and stored simultaneously during the calibration data measurement and we produce the response of only the antenna and the cable as

$$\mathbf{b}(\theta) = \text{diag}(\boldsymbol{\Gamma}_{\text{cal}})^{-1}\mathbf{G}\cdot\mathbf{u}(\theta). \tag{12}$$

At measurement site, the receiver response is measured again and we can produce a new array manifold on measurement site as

$$\hat{\mathbf{a}}_{\text{site}}(\theta) = \text{diag}(\boldsymbol{\Gamma}_{\text{site}})\cdot\mathbf{b}(\theta) \tag{13}$$

$$= \text{diag}(\boldsymbol{\Gamma}_{\text{site}})\cdot\text{diag}(\boldsymbol{\Gamma}_{\text{cal}})^{-1}\mathbf{G}\cdot\mathbf{u}(\theta), \tag{14}$$

where $\mathbf{\Gamma}_{\text{site}}$ denotes the receiver response on measurement site. In beamforming, the mode vector $\mathbf{a}(\theta)$ in (4) is replaced by (14).

On the other hand, in order to obtain the response of the receiver, we input the receiver calibration signal, $s_{\text{cal}}^{\text{rx}}(t)$, by using one-to-eight power divider with the response of $\mathbf{D} = [D_1, D_2, \ldots, D_M]^T \in \mathbb{C}^{M\times 1}$. The array output data is written by

$$\overline{\mathbf{X}}_{\text{cal}}^{\text{rx}}(t) = \mathbf{C}_{\text{cal}} \cdot s_{\text{cal}}^{\text{rx}}(t) + \mathbf{n}(t), \tag{15}$$

where

$$\mathbf{C}_{\text{cal}} = \text{diag}(\mathbf{D}) \cdot \mathbf{\Gamma} \tag{16}$$

$$= ||\mathbf{C}_{\text{cal}}|| \cdot \mathbf{e}_{\text{cal}}, \tag{17}$$

where $\mathbf{e}_{\text{cal}}$ denotes the eigen vector corresponding to the maximum eigen value λ_{cal} of $\mathbf{R}_{\text{cal}} = E[\overline{\mathbf{X}}_{\text{cal}}^{\text{rx}}(t) \cdot \overline{\mathbf{X}}_{\text{cal}}^{\text{rx}}(t)^H]$. If the signal-to-noise ratio (SNR) is large enough, λ_{cal} can be approximated by

$$\lambda_{\text{cal}} \approx ||\mathbf{C}_{\text{cal}}||^2 \cdot P_{\text{cal}}, \tag{18}$$

where P_{cal} means the absolute input power level of the reference signal from the signal generator. By substituting (18) into (17), the receiver response, $\mathbf{\Gamma}$, can be obtained as

$$\mathbf{\Gamma} = \text{diag}(\mathbf{D})^{-1} \mathbf{e}_{\text{cal}} \cdot \sqrt{\lambda_{\text{cal}}/P_{\text{cal}}}. \tag{19}$$

For precise verification of the ETC signal specification, we calculated the absolute received power level applying equivalent isotropic received power (e.i.r.p.).

4. Virtual Reality Modeling Language; VRML

This study proposes the scattering object identification method using 3D visualization with the virtual reality modeling language (VRML) which is the language for displaying 3D objects with a VRML viewer. In some literatures, VRML has been used for the modeling tool for visualization [8] and simulation [9]. However, the significant feature of this study is that VRML is made use of for the purpose of scattering object identification based on the experiment.

Since the popularization of world wide web (WWW), there has been an effort to enhance the content of web documents with advanced 3D graphics and interaction with them. The term virtual reality markup language (VRML) was first used at a European web conference in 1994 where a need for a 3D web standard was addressed. Afterward, the name of the standard was changed to virtual reality modeling language to emphasize the role of graphics.

The brief history review of VRML is well described in [8] as following. The VRML1.0 specification was originated from the prototype 3D web interface "Labyrinth," developed in 1994. The open inventor ASCII file format from Silicon Graphics Inc. was the basis of VRML1.0. This first release of VRML supports the complete description and manipulation of 3D static scenes. The VRML architecture group (VAG) formed in 1995 issues the RFP (request for proposal) for VRML2.0, which was officially released at the Siggraph 96 conference. In 1997 VRML2.0 was stated as an International Standard: VRML97. Now animation, viewpoint binding, texture animation, timers and scripting are Now animation, viewpoint binding, texture animation, timers and scripting are supported, making advanced 3D web content possible. In 1999 the Web 3D consortium joins the W3C (WWW consortium) to form X3D (extensible 3D) as the next generation VRML standard, being fully compatible with VRML97 content and based on XML (extensible markup language).

VRML is a scene graph-based 3D system. All information that defines a 3D scene is stored in so-called "nodes" of the graph. Most of the nodes have special purposes, like holding geometry data, appearance information or transformation rules. VRML includes an event oriented system which enables the nodes to interact with each other and with the user. Because it is a fully descriptive ASCII code language, VRML files can easily be produced and edited by any text editor.

The VRML97 standard continues to be improved by the Web 3D consortium. The newly released X3D standard is the successor to VRML97. X3D is an extensible standard that provides compatibility with existing VRML content and browsers [10].

5. Scattering Object Identification by 3D Visualization

5.1. Basic Idea. In ETC gate environment, propagation mechanism including specular reflection, edge diffraction, corner diffraction and non-specular scattering as well as direct wave can be considered. However, in general, the other paths than direct and specular reflection paths are comparatively weak. For the specular reflection, the image method can be applied to the identification of the equivalent source location that can be found by the measurement data at different positions in the same manner as the direct waves.

Figure 10 shows the coordinate system assumed in the measurement where the origin denotes the starting point of the measurement and the vehicle moves along the x-axis. When the equivalent source location can be represented by (x_0, y_0, z_0), the AoA at the location x is denoted by $\theta_0(x)$. This system computes the 1D beamforming with an eight-element linear antenna array. The power intensity distribution for the AoA along x-axis can be obtained by the beamforming processing.

An infinite number of equivalent sources at $\theta_0(x)$ exist on the conical surface and the observation point becomes its vertex as shown in Figure 10. Hence the equivalent source cannot be uniquely determined, which is called *cone ambiguity*. If it can be uniquely determined, we can identify the scattering object by tracing the peaks on the beamforming spectrum along moving path and approximating to the curve from the relationship of $\theta_0(x) = \cos^{-1}(z_0/\sqrt{(x-x_0)^2 + y_0^2 + z_0^2})$. However, this method is applicable only if the length of the lit zone is sufficiently long

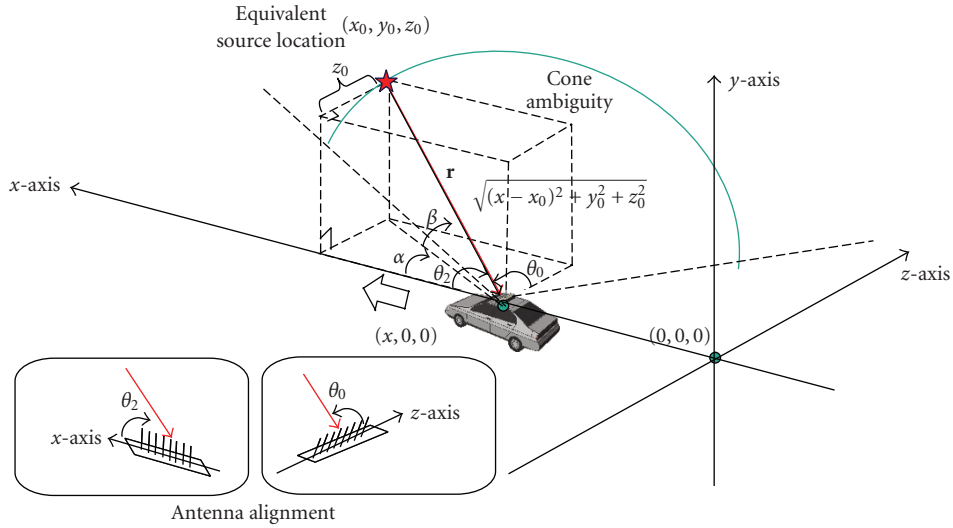

Figure 10: Coordinate system.

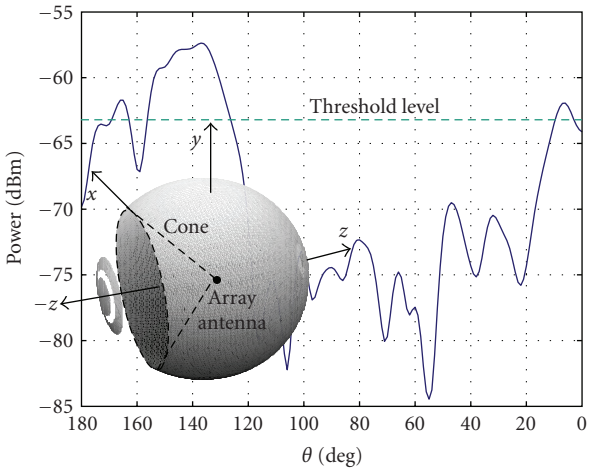

Figure 11: 3D spherical beampattern.

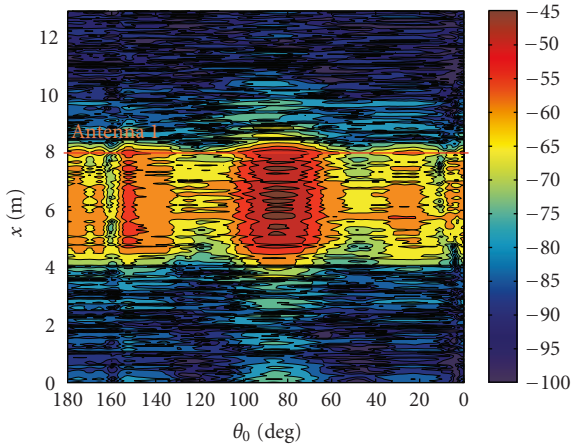

(a) Power intensity distribution (dBm)

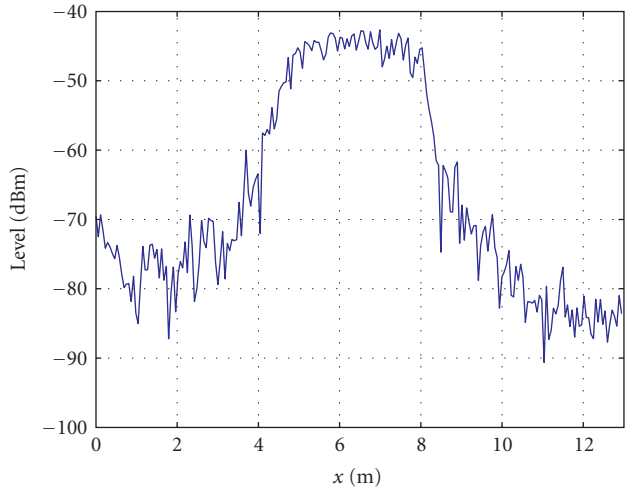

(b) Peak power distribution (dBm)

Figure 12: Power intensity distribution in ETC lane; the transmitter antenna of the roadside station was located at $x = 8$ m.

that we can observe a change of AoA in the beamforming spectrum.

Therefore, this paper proposes the scattering object identification method using 3D visualization of the beamforming results that include the directional signal power intensity along the moving direction (x-axis). An easy way to apply the beamforming results is producing a spherical beampatterns that express the corresponding power intensity by its transparency in a conical pattern on its surface. It means making any parts of the surface transparent when the power is higher than a threshold value and making them colored otherwise. When producing the spherical beampattern, the threshold level should be appropriately chosen. For example, the spherical beampattern produced in 3D graphics is illustrated in Figure 11. Being drawn over the 3D model of the toll gate, the spherical beampattern is converted to VRML and manual identification by human eye keeping the viewpoint at the center of the spherical beampattern is carried out in the VRML viewer.

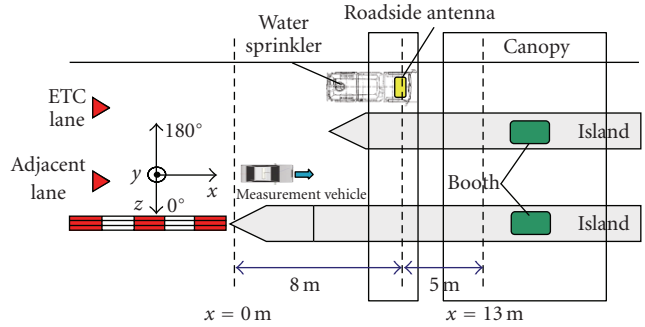

(a) Top view of the gate

(b) Photograph of the measurement

FIGURE 13: Measurement situation on the adjacent lane in case of water sprinkler exits in ETC lane.

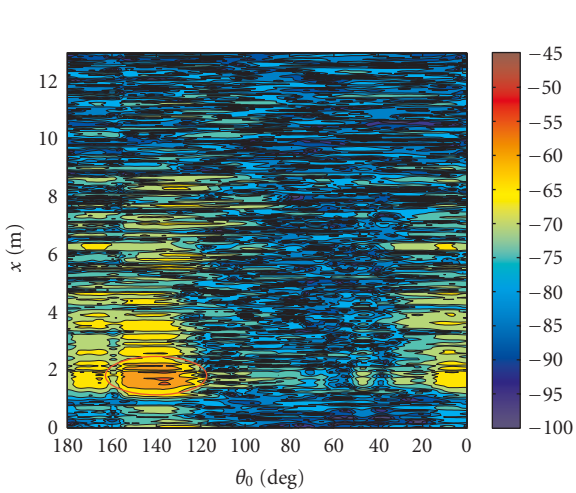

(a) Power intensity distribution (dBm)

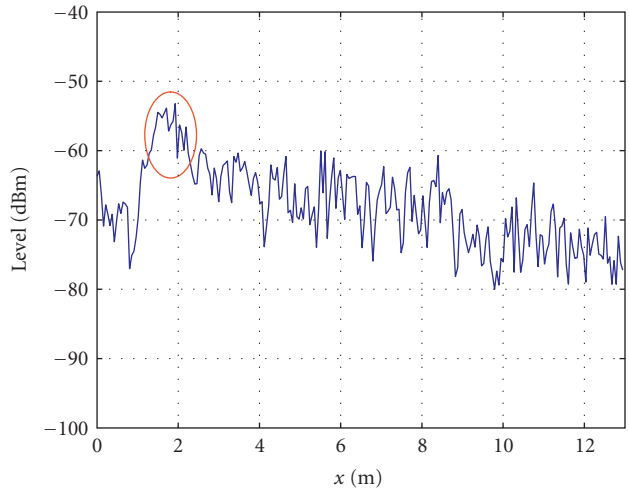

(b) Peak power distribution (dBm)

FIGURE 14: Power intensity distribution on the adjacent lane in case of water sprinkler exits in ETC lane; large leaked power about −55 dBm at around $x = 2$ m and $\theta_0 = 140^\circ$ was found in the circled area.

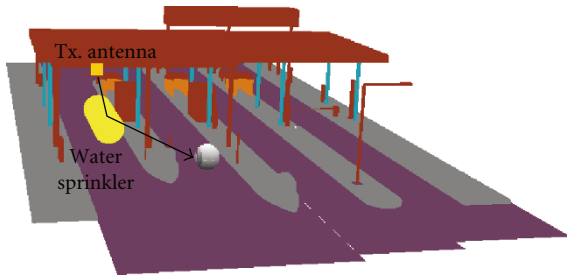

FIGURE 15: 3D visualized results in VRML viewer (perspective view).

5.2. VRML File Generation and Manipulation Procedure. In this study, MATLAB, Mathworks, was used for producing the spherical beampatterns and VRML file generation. The virtual reality toolbox product uses VRML97 standard (VRML2.0) to deliver a unique, open 3D visualization solution for MATLAB.

The step-by-step operation flow in generating VRML file for the scattering object identification is as following. We used the 3D toll gate model drawn by a commercial schematic tool of SketchUp [11] as an execution drawing.

(1) *Import model in MATLAB.* The toll gate model is converted into 3ds format to import to graphics in MATLAB. In importing procedure, some extra steps are required. Several user-contributed open sources available at the MATLAB Central web site [12]. One of them, model3d was used to import the model. It can support Autocad (.dxf) and 3D Studio Max (.3ds) formats (model3d was contributed by Steven Michael of the MIT Lincoln Laboratory).

(2) *Overdraw spherical beampattern.* Draw the spherical beampattern at the exact measurement position over the gate model in MATLAB.

(3) *Save as VRML.* Save as the VRML format using the standard "vrml" function of MATLAB.

(4) *Edit viewpoint and orientation.* In generated VRML model, the viewpoint and orientation is manually edited by applying the measurement position (viewpoint) and view angle (orientation) by any text editor.

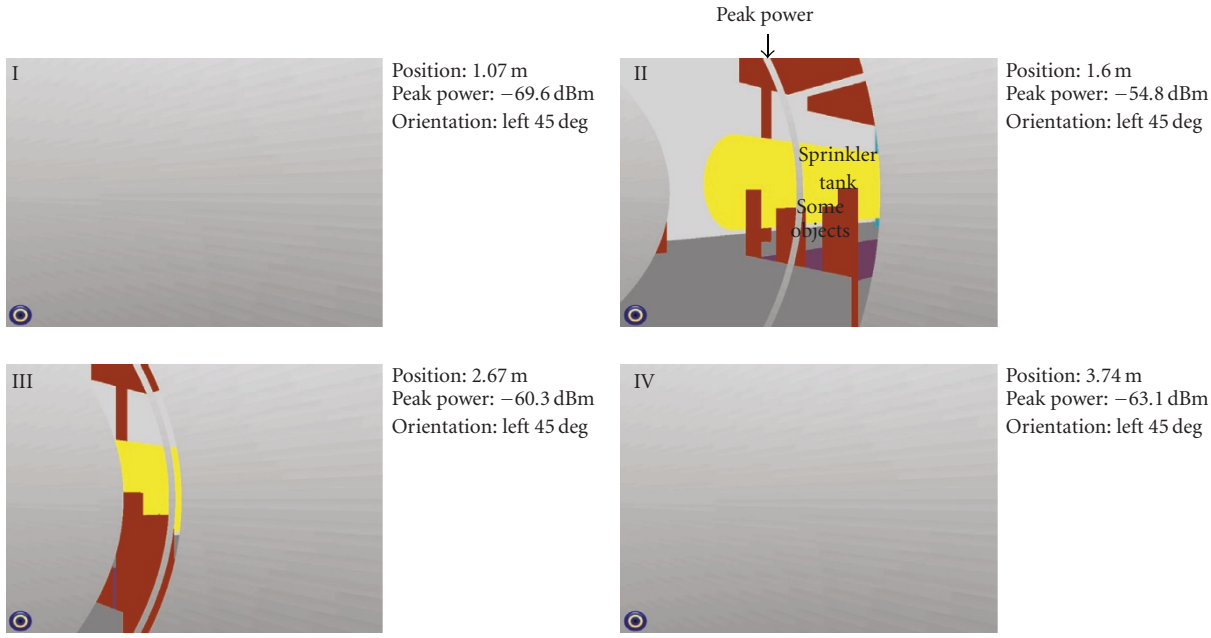

(a) Threshold level: −60.5 dBm

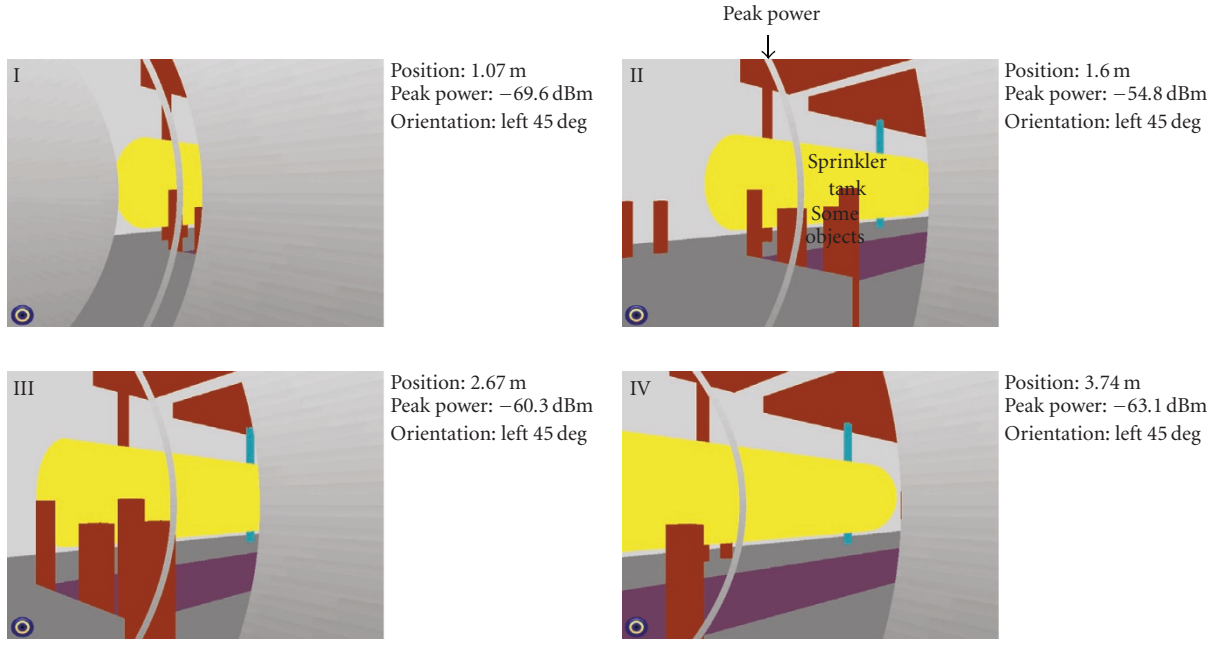

(b) Threshold level: −70.5 dBm

Figure 16: Scenes viewed from the center of the spherical beampatterns in VRML viewer at different positions of 1.07, 1.6, 2.67, and 3.74 m.

(5) *Load on VRML viewer.* There are many free downloadable VRML/X3D viewers. Herein, BS Contact VRML/X3D 7.02, Bitmanagement Software GmbH [13], was used.

(6) *Identify the scattering object.* Some movement operations such as examine, pan, walk, slide, and so forth are available in the VRML viewer. We can see the surroundings through the spherical beampattern at the center of the sphere in virtual reality world.

6. Measurement Examples in ETC Gate

In this section, the measurement results in a highway ETC gate that was not open for traffic yet are presented. Figure 12(a) is the contour plot of the power intensity distribution with respect to the angle θ_0 formed by the array axis and the source direction, which were calculated by beamforming along the ETC lane. The transmitter antenna

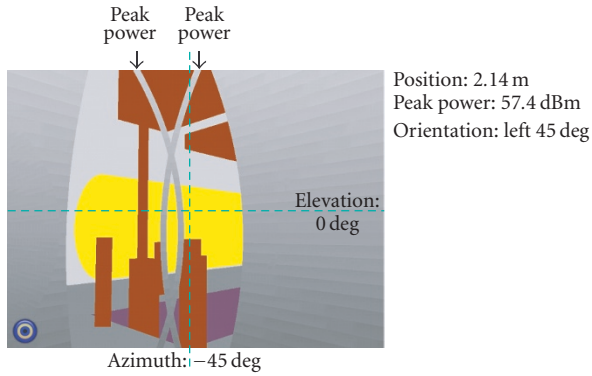

Figure 17: 2D identification by multiple measurements in two different directions of the array axis (simulation).

of the roadside station was located at 8 m from the starting point of the measurement in height of 5.5 m. In ARIB-T75 standard, the communication zone is specified by 4 m from the position directly below the transmitter antenna [6]. It can be seen that the peak power appears at the transmitter antenna direction (90°) and the transmitting power from the roadside station is well confined within the communication zone as shown in Figure 12(b) more apparently.

Over-reach problems caused by scattering in ETC lane have been studied in [2, 4]. For example, if the car is passing through the ETC gate and a big object like water sprinkler is also passing through the adjacent ETC lane at the same time, the signal power can be over-reached out of the specified communication zone due to the scattering and hence the malfunction can occur by this leaked power.

In this experiment, we tried to evaluate the effect of big scattering object. Figure 13 illustrates the measurement situation as the vehicle with the system carries out the measurement passing through the adjacent lane when a water sprinkler exists in the ETC lane. The length of the measurement area was 13 m and the transmitter antenna location in the ETC lane was $x = 8$ m from the starting point of the measurement as the same above. Figure 14 presents the measurement results on the adjacent lane. Figure 14(a) shows the power intensity distribution. From this results, we can find large leaked power about −55 dBm in the adjacent lane caused by the scattering of the water sprinkler at around $x = 2$ m and $\theta_0 = 140$ deg. It means that the malfunction can occur by this leaked signal because the threshold power level in the ETC receiver operation is prescribed by −70.5 dBm.

Figure 15 shows the perspective view of the 3D visualized results in VRML viewer. It was generated by the procedure mentioned in Section 5.2. The resulting scenes viewed from the center of the spherical beampatterns at four different measurement positions (1.07, 1.6, 2.67, and 3.74 m) are shown in Figure 16(a) and Figure 16(b), where the threshold levels in producing the spherical beampattern were set by the lower bound of the ordinary receiving power, −60.5 dBm and the operation threshold, −70.5 dBm, respectively. It can be seen that the tank of the water sprinkler is identified as a scattering object and the corresponding power intensity is also easily found.

7. Discussions

This system employed a linear array antenna with finite number of elements and computed the 1D beamforming for the array axis. To improve the identification resolution, multiple measurements changing the direction of the array axis can be considered. For example, if an additional beamforming is done horizontally to the moving direction (x-axis) as shown in Figure 10, the 2D (azimuth and elevation) identification becomes possible using the vertical beamforming (z-axis) as well that considered so far.

Although two crossing lines formed by two conical surfaces from each measurement are obtained, the line above ground can be uniquely determined because the reception by ground reflection is negligible in this antenna geometry. However, if there are n sources, n^2 candidates can exist, thus the identification complexity will greatly increase.

Figure 17 shows an example by computer simulation. In this simulation, it is assumed that the AoAs estimated by two measurements for z-axis and x-axis are $(\theta_0, \theta_2) = (140^\circ, 50^\circ)$, respectively. From the conversion relationship in Appendix, azimuth and elevation can be calculated as $(\alpha, \beta) = (-50^\circ, 0^\circ)$.

On the other hand, in this study, the identification method using 3D models was proposed. However, as a matter of fact, the 3D models are not always available. To answer this practical question, it can be also thought to use the pictures of the panorama view of the gate taken synchronously to the data capture timing by a fish-eye camera as in [14] instead of 3D model of the toll gate. It typically needs the hardware reconfiguration, and hence, in this time, the further evaluation remains as a future study.

8. Conclusion

This paper proposed a novel real-time radio propagation measurement system for the ETC toll gates without closing the gate. The measurement can be made on the vehicle passing through the gates using real ETC signal transmitted by ETC roadside station. This system can obtain the angular power intensity distribution around the ETC gate in real time and identify the individual scattering object with 3D visualization method based on VRML. We also proposed a 3D visualization based identification method for the individual scattering object. Moreover, the validity of the system and identification method was demonstrated by the field experiment in a highway ETC gate.

Appendix

Azimuth and Elevation Conversion Relationship

In Figure 10, the relations between the directional vector of a source and the unit vectors of z- and x-axes are expressed as

$$\mathbf{r}\cdot\mathbf{z} = \cos\theta_0, \tag{A.1}$$

$$\mathbf{r}\cdot\mathbf{x} = \cos\theta_2. \tag{A.2}$$

From the relation between polar and Cartesian coordinate systems, (A.1) and (A.2) can be rewritten as

$$\mathbf{r}\cdot\mathbf{z} = \cos\beta\cdot\cos\alpha, \tag{A.3}$$

$$\mathbf{r}\cdot\mathbf{x} = \cos\beta\cdot\sin\alpha. \tag{A.4}$$

By substituting (A.3) and (A.4) with (A.1) and (A.2), respectively,

$$\cos\theta_0 = \cos\beta\cdot\cos\alpha, \tag{A.5}$$

$$\cos\theta_2 = \cos\beta\cdot\sin\alpha. \tag{A.6}$$

By (A.6)/(A.5),

$$\tan\alpha = \frac{\cos\theta_2}{\cos\theta_0}. \tag{A.7}$$

And by $(\text{A.6})^2 + (\text{A.5})^2$, we can obtain the relation as

$$\cos\beta = \cos^2\theta_0 + \cos^2\theta_2. \tag{A.8}$$

From above relations, azimuth α and elevation β are obtained from θ_0 and θ_2 by

$$\begin{aligned} \alpha &= \tan^{-1}\frac{\cos\theta_0}{\cos\theta_2} \quad (|\alpha| \le \pi/2), \\ \beta &= \cos^{-1}\sqrt{\cos^2\theta_0 + \cos^2\theta_2} \quad (0 \le \beta \le \pi/2). \end{aligned} \tag{A.9}$$

Acknowledgments

The authors would like to thank East Nippon Expressway Company Limited for the support during the field measurements in Kasama Nishi IC. The authors would also like to express the appreciation to Mr. K. Ri, Mr. Y. Choi, and T. Kan for their help in the experiment.

References

[1] Homepage of Ministry of Land, Infrastructure, Transport and Tourism, Japan, http://www.mlit.go.jp/road/ITS/.

[2] H. Kurihara, Y. Hirai, K. Takizawa, T. Iwata, and O. Hashimoto, "An improvement of communication environment for ETC system by using transparent EM wave absorber," *IEICE Transactions on Electronics*, vol. E88-C, no. 12, pp. 2350–2357, 2005.

[3] T. Iwata, Y. Wakinaka, and J.-I. Takada, "Experimental identification of undesired propagation paths for ETC," in *Proceedings of the 2nd International Workshop on ITS Telecommunications (ITST '01)*, pp. 131–136, Yokosuka, Japan, October 2001.

[4] K. Haneda, J.-I. Takada, T. Iwata, and Y. Wakinaka, "Experimental determination of propagation paths for the ETC system—equipment development and field test," *IEICE Transactions on Fundamentals of Electronics, Communications and Computer Sciences*, vol. E87-A, no. 11, pp. 3008–3015, 2004.

[5] K. Mizutani, K. Sakaguchi, J.-I. Takada, and K. Araki, "Development of MIMO-SDR platform and its application to real-time channel measurements," *IEICE Transactions on Communications*, vol. E89-B, no. 12, pp. 3197–3207, 2006.

[6] "Dedicated short-range communication system," *ARIB Standard*, ARIB STD-T75, Association of Radio Industries and Businesses, 2001.

[7] F. Belloni, A. Richter, and V. Koivunen, "DoA estimation via manifold separation for arbitrary array structures," *IEEE Transactions on Signal Processing*, vol. 55, no. 10, pp. 4800–4810, 2007.

[8] M. Bartsch, M. Clemens, T. Hippler, and T. Weiland, "Advanced electromagnetic field visualization using the virtual reality modeling language standard," *IEEE Transactions on Magnetics*, vol. 37, no. 5 I, pp. 3604–3607, 2001.

[9] T. Hattori and T. Kato, "Analyses of propagation characteristics by VRML models along railway," in *Proceedings of the 60th IEEE Vehicular Technology Conference (VTC '04)*, vol. 6, pp. 4233–4237, Los Angeles, Calif, USA, 2004.

[10] Web 3D consortium, http://www.web3d.org.

[11] Google SketchUp, Google, http://sketchup.google.com.

[12] MATLAB Central, Mathworks, http://www.mathworks.com/matlabcentral.

[13] BS Contact VRML/X3D 7.02, VRML Viewer software, Bitmanagement Software GmbH, http://www.bitmanagement.com/.

[14] N. Lertsirisopon, G. S. Ching, M. Ghoraishi, J.-I. Takada, and I. Ida, "Directional channel characteristics from microcell measurement and simulation," in *Proceedings of Asia-Pacific Microwave Conference (APMC '07)*, pp. 1–4, Bangkok, Thailand, December 2007.